# Systematic study of Si-based GeSn photodiodes with 2.6 µm detector cutoff for short-wave infrared detection

**Thach Pham,[1] Wei Du,[1,*] Huong Tran,[1] Joe Margetis,[2] John Tolle,[2] Greg Sun,[3] Richard A. Soref,[3] Hameed A. Naseem,[1] Baohua Li,[4] and Shui-Qing Yu[1]**

[1]*Department of Electrical Engineering, University of Arkansas, Fayetteville, AR 72701, USA*
[2]*ASM, Phoenix, AZ 85034, USA*
[3]*Department of Engineering, University of Massachusetts Boston, Boston, MA 02125, USA*
[4]*Arktonics LLC, Fayetteville, AR 72701, USA*
**weidu@uark.edu*

**Abstract:** Normal-incidence $Ge_{1-x}Sn_x$ photodiode detectors with Sn compositions of 7 and 10% have been demonstrated. Such detectors were based on Ge/$Ge_{1-x}Sn_x$/Ge double heterostructures grown directly on a Si substrate via a chemical vapor deposition system. A temperature-dependence study of these detectors was conducted using both electrical and optical characterizations from 300 to 77 K. Spectral response up to 2.6 µm was achieved for a 10% Sn device at room temperature. The peak responsivity and specific detectivity (D*) were measured to be 0.3 A/W and $4 \times 10^9$ cmHz$^{1/2}$W$^{-1}$ at 1.55 µm, respectively. The spectral D* of a 7% Sn device at 77 K was only one order-of-magnitude lower than that of an extended-InGaAs photodiode operating in the same wavelength range, indicating the promising future of GeSn-based photodetectors.

©2016 Optical Society of America

**OCIS codes:** (040.5160) Photodetectors; (130.3120) Integrated optics devices; (310.1860) Deposition and fabrication; (230.5160) Photodetectors.

## References and links

1. N. K. Dhar, R. Dat, and A. K. Sood, "Advances in Infrared Detector Array Technology," in *Optoelectronics - Advanced Materials and Devices*, S. L. Pyshkin and J. M. Ballato, eds. (Intech, 2013).
2. A. Rogalski, "Infrared detectors: an overview," Infrared Phys. Technol. **43**(3), 187–210 (2002).
3. A. Rogalski, "Progress in focal plane array technologies," Prog. Quantum Electron. **36**(2-3), 342–473 (2012).
4. H. H. Cheng, Private communication, National Taiwan University (November 2015).
5. R. Roucka, J. Xie, J. Kouvetakis, J. Mathews, V. D'Costa, J. Menendez, J. Tolle, and S. Q. Yu, "$Ge_{1-y}Sn_y$ photoconductor structures at 1.55 µm: From advanced materials to prototype devices," J. Vac. Sci. Technol. B **26**(6), 1952–1959 (2008).
6. M. Coppinger, J. Hart, N. Bhargava, S. Kim, and J. Kolodzey, "Photoconductivity of germanium tin alloys grown by molecular beam epitaxy," Appl. Phys. Lett. **102**(14), 141101 (2013).
7. B. R. Conley, J. Margetis, W. Du, H. Tran, A. Mosleh, S. A. Ghetmiri, J. Tolle, G. Sun, R. Soref, B. Li, H. A. Naseem, and S.-Q. Yu, "Si based GeSn photoconductors with a 1.63 A/W peak responsivity and a 2.4 µm longwavelength cutoff," Appl. Phys. Lett. **105**(22), 221117 (2014).
8. B. R. Conley, A. Mosleh, S. A. Ghetmiri, W. Du, R. A. Soref, G. Sun, J. Margetis, J. Tolle, H. A. Naseem, and S. Q. Yu, "Temperature dependent spectral response and detectivity of GeSn photoconductors on silicon for short wave infrared detection," Opt. Express **22**(13), 15639–15652 (2014).
9. T. N. Pham, W. Du, B. R. Conley, J. Margetis, G. Sun, R. Soref, J. Tolle, B. Li, and S.-Q. Yu, "Si-based $Ge_{0.9}Sn_{0.1}$ photodetector with peak responsivity of 2.85 A/W and longwave cutoff at 2.4 µm," Electron. Lett. **51**(11), 854–856 (2015).
10. D. Zhang, C. Xue, B. Cheng, S. Su, Z. Liu, X. Zhang, G. Zhang, C. Li, and Q. Wang, "High-responsivity GeSn short-wave infrared p-i-n photodetectors," Appl. Phys. Lett. **102**(14), 141111 (2013).
11. A. Gassenq, F. Gencarelli, J. Van Campenhout, Y. Shimura, R. Loo, G. Narcy, B. Vincent, and G. Roelkens, "GeSn/Ge heterostructure short-wave infrared photodetectors on silicon," Opt. Express **20**(25), 27297–27303 (2012).

#255681 Received 14 Dec 2015; revised 12 Feb 2016; accepted 19 Feb 2016; published 23 Feb 2016

12. S. Kim, J. Gupta, N. Bhargava, M. Coppinger, and J. Kolodzey, “Current-Voltage Characteristics of GeSn/Ge Heterojunction Diodes Grown by Molecular Beam Epitaxy,” IEEE Electron Device Lett. **34**(10), 1217–1219 (2013).
13. J. Mathews, R. Roucka, J. Xie, S. Yu, J. Menéndez, and J. Kouvetakis, “Extended performance GeSn/Si(100) p-i- n photodetectors for full spectral range telecommunication applications,” Appl. Phys. Lett. **95**(13), 133506 (2009).
14. J. Werner, M. Oehme, M. Schmid, M. Kaschel, A. Schirmer, E. Kasper, and J. Schulze, “Germanium-tin p-i-n photodetectors integrated on silicon grown by molecular beam epitaxy,” Appl. Phys. Lett. **98**(6), 061108 (2011).
15. S. Su, B. Cheng, C. Xue, W. Wang, Q. Cao, H. Xue, W. Hu, G. Zhang, Y. Zuo, and Q. Wang, “GeSn p-i-n photodetector for all telecommunication bands detection,” Opt. Express **19**(7), 6400–6405 (2011).
16. Y.-H. Peng, H. H. Cheng, V. I. Mashanov, and G.-E. Chang, “GeSn p-i-n waveguide photodetectors on silicon substrates,” Appl. Phys. Lett. **105**(23), 231109 (2014).
17. H. H. Tseng, H. Li, V. Mashanov, Y. J. Yang, H. H. Cheng, G. E. Chang, R. A. Soref, and G. Sun, “GeSn based p-i-n photodiodes with strained active layer on a Si wafer,” Appl. Phys. Lett. **103**(23), 231907 (2013).
18. M. Oehme, K. Kostecki, K. Ye, S. Bechler, K. Ulbricht, M. Schmid, M. Kaschel, M. Gollhofer, R. Körner, W. Zhang, E. Kasper, and J. Schulze, “GeSn-on-Si normal incidence photodetectors with bandwidths more than 40 GHz,” Opt. Express **22**(1), 839–846 (2014).
19. R. Roucka, J. Mathews, C. Weng, R. Beeler, J. Tolle, J. Menendez, and J. Kouvetakis, “High-Performance Near-IR Photodiodes: A Novel Chemistry-Based Approach to Ge and Ge–Sn Devices Integrated on Silicon,” IEEE J. Quantum Electron. **47**(2), 213–222 (2011).
20. Y. Dong, W. Wang, D. Lei, X. Gong, Q. Zhou, S. Y. Lee, W. K. Loke, S. F. Yoon, E. S. Tok, G. Liang, and Y. C. Yeo, “Suppression of dark current in germanium-tin on silicon p-i-n photodiode by a silicon surface passivation technique,” Opt. Express **23**(14), 18611–18619 (2015).
21. J. Margetis, S. A. Ghetmiri, W. Du, B. R. Conley, A. Mosleh, R. A. Soref, G. Sun, L. Domulevicz, H. A. Naseem, S. Q. Yu, and J. Tolle, “Growth and characterization of epitaxial $Ge_{1-X}Sn_x$ alloys and heterostructures using a commercial CVD system,” ECS Trans. **64**(6), 711 (2014).
22. S. S. Hegedus and W. N. Shafarman, “Thin-film solar cells: device measurements and analysis,” Prog. Photovolt. Res. Appl. **12**(23), 155–176 (2004).
23. J. R. Sites and P. H. Mauk, “Diode quality factor determination for thin-film solar cells,” Solar Cells. **27**(1), 411–417 (1989).
24. A. Rogalski, *Infrared detectors* (CRC, 2010).
25. H. W. Yoon, M. C. Dopkiss, and G. P. Eppeldauer, “Performance comparisons of InGaAs, extended InGaAs, and short-wave HgCdTe detectors between 1 μm and 2.5 μm,” Proc. SPIE **6297**, 629703 (2006).
26. W. Shockley and W. T. Read, Jr., “Statistics of the recombinations of holes and electrons,” Phys. Rev. **87**(5), 835–842 (1952).
27. Z. Huang, J. Oh, S. K. Banerjee, and J. C. Campbell, “Effectiveness of SiGe buffer layers in reducing dark currents of Ge-on-Si photodetectors,” IEEE J. Quantum Electron. **43**(3), 238–242 (2007).
28. G. Karve, S. Wang, F. Ma, X. Li, J. C. Campbell, R. G. Ispasoiu, D. S. Bethune, W. P. Risk, G. S. Kinsey, J. C. Boisvert, T. D. Isshiki, and R. Sudharsanan, “Origin of dark counts in $In_{0.53}Ga_{0.47}As/In_{0.52}Al_{0.48}As$ avalanche photodiodes operated in Geiger mode,” Appl. Phys. Lett. **86**(6), 063505 (2005).
29. C. Lu, C. H. Lee, T. Nishimura, and A. Toriumi, “Yttrium scandate thin film as alternative high-permittivity dielectric for germanium gate stack formation,” Appl. Phys. Lett. **107**(7), 072904 (2015).
30. S. A. Ghetmiri, W. Du, B. R. Conley, A. Mosleh, A. Nazzal, G. Sun, R. A. Soref, J. Margetis, T. Joe, H. A. Naseem, and S. Q. Yu, “Shortwave-infrared photoluminescence from $Ge_{1-x}Sn_x$ thin films on silicon,” J. Vac. Sci. Technol. B **32**(6), 060601 (2014).
31. N. Peyghambarian, S. W. Koch, and A. Mysyrowicz, *Introduction to Semiconductor Optics* (Prentice Hall, 1993).
32. V. Sorianello, A. De Iacovo, L. Colace, A. Fabbri, L. Tortora, E. Buffagni, and G. Assanto, “High responsivity near-infrared photodetectors in evaporated Ge-on-Si,” Appl. Phys. Lett. **101**(8), 081101 (2012).
33. M. Oehme, K. Kostecki, M. Schmid, M. Kaschel, M. Gollhofer, K. Ye, D. Widmann, R. Koerner, S. Bechler, E. Kasper, and J. Schulze, “Franz-Keldysh effect in GeSn pin photodetectors,” Appl. Phys. Lett. **104**(16), 161115 (2014).
34. S. M. Sze and K. K. Ng, *Physics of Semiconductor Devices* (John Wiley & Sons, 2006).


## 1. Introduction

GeSn techniques have drawn much attention recently because the operation range of GeSn-based optoelectronic devices can cover the near- and short-wave infrared (NIR, SWIR) wavelengths desirable for Si photonics. Particularly, research activities in GeSn detectors have experienced a strong increase in the past five years. Developing high-performance GeSn detectors is strongly motivated by these facts: 1) the market-dominating detectors operating in the SWIR wavelength range rely mainly upon III-V (such as InGaAs and InSb and HgCdTe) techniques [1,2], that are incompatible with Si complementary metal-oxide-semiconductor

#255681 Received 14 Dec 2015; revised 12 Feb 2016; accepted 19 Feb 2016; published 23 Feb 2016
© 2016 OSA

(CMOS) processes, resulting in limited sizes of focal plane arrays (FPAs) and high cost; 2) the GeSn technique offers a viable low-cost solution at these wavelengths for large-scale FPAs monolithically integrated on Si; 3) owing to the tremendous effort made to develop material growth including chemical vapor deposition (CVD) and molecular beam epitaxy (MBE), device-level material quality of GeSn has been achieved; 4) our previous study showed 2.4 µm photo-response cutoff with a responsivity of 2.85 A/W at 1.55 µm and 77 K from a 10% Sn photoconductor, which exceeded the Ge (0.8 A/W) and InGaAs (1.0 A/W) photovoltaic detectors operating at the same wavelength [2,3]; 5) an uncooled GeSn detector FPA (256 × 256 upon a readout integrated circuit) has been achieved recently [4]. For the past five years, multiple $Ge_{1-x}Sn_x$ detectors have been designed and fabricated and their characteristics have been investigated [5–20]. In order to improve the device performance in terms of spectral response and specific detectivity (D*), the GeSn photodiode with high Sn composition and low dark current is preferred. Some preliminary results on GeSn photodiodes have been reported recently [10–20]. In this work, a systematic study of the $Ge/Ge_{1-x}Sn_x/Ge$ double heterostructure (DHS) photodiode with Sn compositions of 7 and 10% has been conducted. The current-voltage characteristics, spectral response and responsivity have been characterized at the temperatures from 300 to 77 K. Spectral response wavelength cutoff at 2.6 µm and peak responsivity of 0.3 A/W were observed. Moreover, the carrier activation energy and noise current were evaluated, based on which the spectral D* was obtained. The D* of photodiode with 7% Sn at 77 K showed only one order-of -magnitude lower value than that of extended-InGaAs photodetectors operating in the same wavelength range.

## 2. Device preparation

The GeSn DHS samples were grown using an ASM Epsilon® 2000-plus reduced- pressure chemical vapor deposition system. Figure 1(a) shows the schematic cross sectional view of the device structure, composed of a 750-nm-thick p-type Ge layer (also serving as the buffer layer), a 200-nm-thick unintentionally doped $Ge_{1-x}Sn_x$ active layer, and a 50-nm-thick n-type Ge cap layer. Since the unintentionally doped GeSn layer was measured to be slightly p-type doped, in order to achieve a good p-n junction, the doping concentrations for p-type and n-type Ge layers were chosen as $5 \times 10^{18}$ and $1 \times 10^{19}$ $cm^{-3}$, respectively. The relaxed p-type Ge layer was grown by a two-step growth method. Since the introduction of boron doping leads to the degradation of Ge seed layer quality, firstly an undoped 150 nm Ge seed layer was grown at < 400°C in $H_2$ carrier gas using $GeH_4$ as precursor at the partial pressure of 0.2 torr. The temperature was then increased to 600 °C at a ramp rate of 1 °C/min while keeping the $GeH_4$ partial pressure, followed by the introduction of 1% $B_2H_6$ as the boron doping source once the temperature stabilized at 600 °C. A post growth *in situ* anneal was done at > 800 °C, which reduced the threading dislocations and re-distributed the boron dopant more evenly across the entire p-type Ge layer.

The chamber was then cooled down to < 350 °C in $H_2$ ambience for GeSn layer growth. The $SnCl_4$ and $GeH_4$ were used as Sn and Ge precursors, respectively. The $GeH_4/SnCl_4$ molar flow ratio varied between 0.95 and 0.99 depending on the target Ge/Sn composition. The $H_2$ was used as carrier gas at a flow rate of 15 slm. Finally, the 50-nm-thick n-type Ge layer was deposited at the same temperature to avoid Sn-precipitation. $N_2$ carrier gas was used to increase the Ge growth rate at the low growth temperature and 1% $PH_3$ was used as the phosphorous doping source. A detailed study of this growth method was reported elsewhere [21].

#255681 Received 14 Dec 2015; revised 12 Feb 2016; accepted 19 Feb 2016; published 23 Feb 2016
© 2016 OSA

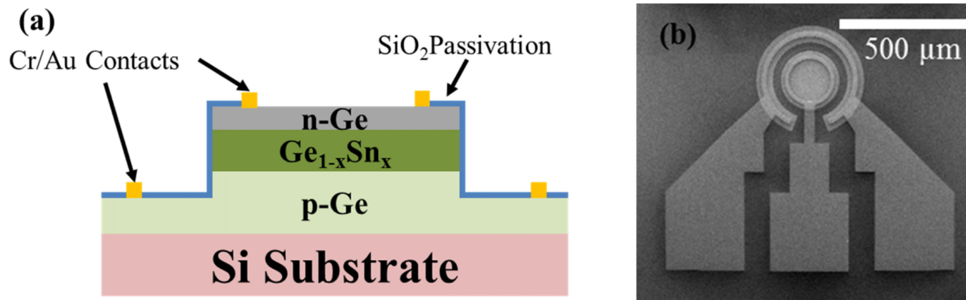


Fig. 1. (a) Schematic cross-sectional view of the device structure. (b) Top view SEM image of 250 μm device.

**Table 1. Sn Composition, Thickness, and Strain for Each Layer.**

| Nominal Sn % | Measured Sn % | p-type Ge thickness (nm) | $Ge_{1-x}Sn_x$ thickness (nm) | n-type Ge thickness (nm) | $Ge_{1-x}Sn_x$ in-plane Strain |
|---|---|---|---|---|---|
| 7.0 | 6.44 | 750 | 200 | 50 | –0.43% |
| 10.0 | 9.24 | 750 | 200 | 50 | –0.48% |

The material quality, layer thickness, and strain of two samples presented in this study were characterized using transmission electron microscopy (TEM) and X-ray diffraction (XRD) techniques. TEM results show the high quality of grown material with defects trapped at Ge/Si interfaces due to the optimized growth of Ge buffer layer, leading to the low-defect GeSn active layer. The XRD-measured Sn compositions of 6.44 and 9.24% are slightly lower than the targets of 7 and 10%, respectively. Further analysis using two-theta omega scan (not shown here) reveals a clear single $Ge_{1-x}Sn_x$ peak for each sample, which suggests the high material quality. The $Ge_{0.9}Sn_{0.1}$ and $Ge_{0.93}Sn_{0.7}$ active layers exhibit the in-plane compressive strain of 0.48 and 0.33%, respectively. The material characterization results are summarized in Table 1.

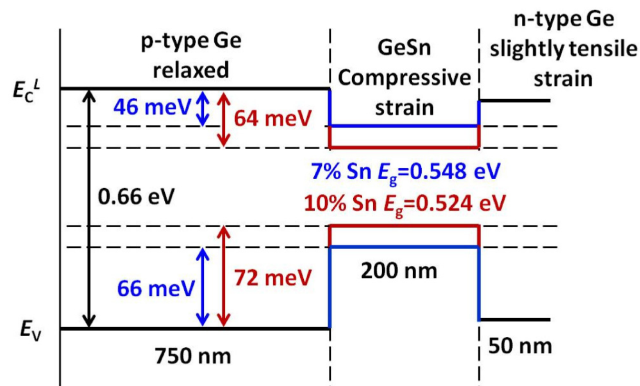


Fig. 2. $Ge/Ge_{1-x}Sn_x/Ge$ DHS band structure (not to scale). Type-I band alignment was formed, which provides a favorable carrier confinement for the device.

Based on our theoretical study, both GeSn layers with 7 and 10% Sn compositions remain indirect bandgap due to the compressive strain (otherwise 10% Sn would exhibit direct bandgap). Incorporation of Sn pushes down the Γ- and L-valleys in the conduction band while lifting the valence band, therefore the type-I alignment of the $Ge/Ge_{1-x}Sn_x/Ge$ DHS is achieved, which favors the carrier confinement. The band structures of 7 and 10% Sn samples are shown in Fig. 2.

#255681 Received 14 Dec 2015; revised 12 Feb 2016; accepted 19 Feb 2016; published 23 Feb 2016
© 2016 OSA

Circular mesa structures with diameters of 250 and 500 μm were fabricated by photolithography and wet chemical etch processes. The solution of HCl: $H_2O_2$: $H_2O$ = 1:1:20 was used for the mesa etching. A stable etching rate of 100 nm/min at room temperature regardless of Sn composition was observed. The etching depth was controlled to be 500 nm to expose the p-type Ge layer for metal contact. A 100-nm-thick $SiO_2$ passivation layer was then deposited by plasma-enhanced chemical vapor deposition followed by the openings made for the metal contacts. Electrode pads were patterned and metalized with 10/200 nm of Cr/Au. The top view scanning electron microscope (SEM) image is shown in Fig. 1(b).

## 3. Measurement methods

The temperature-dependent testing setup is mainly composed of a Janis cryostat using liquid nitrogen cooling and controlled by a Lakeshore cryogenic controller. A chip carrier with wire-bonded devices placed inside cryostat was connected to outside measurement equipment through an isolated BNC feed-through system. The current-voltage characteristic was measured using a Keithley 6487 picoammeter, based on which the electrical parameters such as reverse saturation current, series resistance, and shunt resistance were extracted.

The temperature-dependent spectral response measurement was conducted by using a Fourier-transform infrared (FTIR) spectrometer system. The IR light from the internal source was guided and focused to the sample mounted in the cryostat. Although this method reduces the high-order diffraction ambiguity of full IR spectrum analysis, the radiant flux of the light source remains arbitrary. For the responsivity measurement, a laser diode with a wavelength of 1.55 μm optically chopped at 380 Hz and a lock-in amplifier were used. The optical power of the laser diode was measured using an ILX Lightwave power meter. The absolute responsivity values were calibrated using a NIST traceable InGaAs p-i-n photodiode. Moreover, the D* was calculated based on measured values of responsivity and the dark current.

## 4. Temperature dependent current-voltage characterization

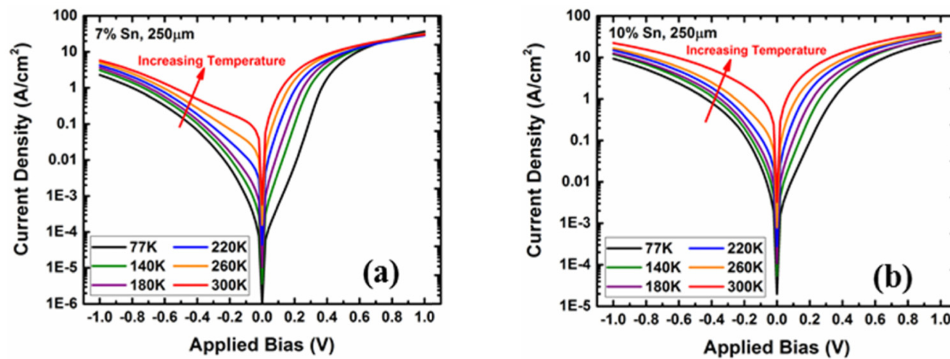


Fig. 3. Temperature dependent I-V characteristic of GeSn photodiode with (a) 7% Sn and (b) 10% Sn. The mesa size is 250 μm in diameter.

Figures 3(a) and 3(b) show the dark current-voltage (I-V) characteristics from 300 to 77 K of the GeSn photodiodes (mesa size of 250 μm in diameter) with Sn compositions of 7 and 10%, respectively. The rectifying diode like behavior was observed on both devices at each temperature. As the temperature increases, the reverse current density increases as a result of more thermally activated carriers. At a certain reverse voltage, the current density of the 10% Sn device is higher than that of the 7% Sn device for each temperature. This is mainly due to the narrower bandgap of the 10% Sn device compared to that of the 7% Sn device due to the higher Sn composition, which results in the more thermally excited carriers.

#255681 Received 14 Dec 2015; revised 12 Feb 2016; accepted 19 Feb 2016; published 23 Feb 2016
© 2016 OSA

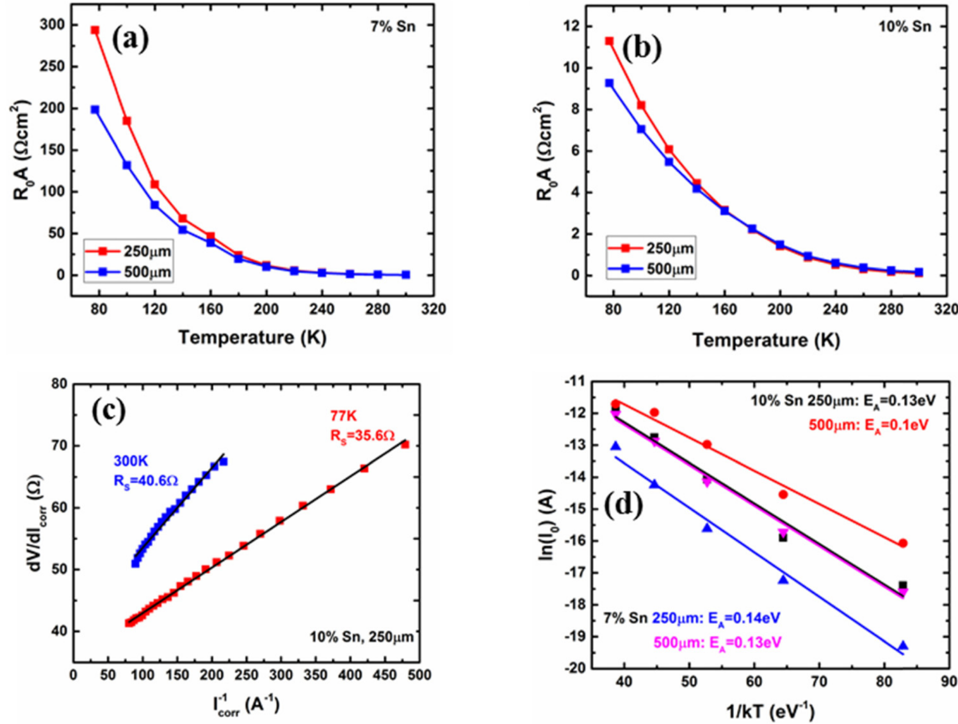


Fig. 4. Zero-bias resistance-area product ($R_0A$) at different temperatures of (a) 7% Sn and (b) 10% Sn devices. (c) Linear fit of $(I_{corr})^{-1}$ as a function of $dV/dI_{corr}$ at 77 and 300 K of the 7% Sn sample. (d) Activation energy of 7 and 10% Sn with different mesa sizes.

The diode current can be expressed as [12]:

$$I = I_0 \exp[\frac{q(V - R_S I_{corr})}{nkT}] + \frac{V}{R_{Sh}} \quad (1)$$

where $I$ is the measured current, $I_0$ is the reverse saturation current, $q$ is the electronic charge, $V$ is the applied voltage, $n$ is the ideality factor, $k$ is the Boltzmann constant, $T$ is the absolute temperature, $R_s$ is the series resistance, $R_{sh}$ is the shunt resistance, and $I_{corr} = I - V/R_{Sh}$ is the corrected diode current (net current flowing through the diode) [12,22,23]. Shunt resistance $R_{sh}$ was first extracted by taking $dI/dV$ near 0 V (where $1/R_{sh}$ dominates other terms) for each temperature. Consequently the zero-bias resistance-area product ($R_0A \approx R_{sh}A$) was calculated with the corresponding device area $A$, as shown in Figs. 4(a) and 4(b). $R_0A$ values of 300 and 11 $\Omega\cdot cm^2$ were obtained at 77 K for 7 and 10% Sn devices, respectively, which are lower values compared to those of InGaAs and HgCdTe detectors [2,24]. The shunt resistance is mainly coming from the following facts: 1) There is surface recombination due to the lack of surface passivation. This part of the shunt resistance can be eliminated by applying passivation technique reported in [20]; 2) Since a wet chemical etching process was used for the mesa etch, some Sn could be re-deposited on the mesa surface and sidewall, resulting in the shunt current.

Replacing $I$ by $I_{corr} = I - V/R_{Sh}$ in Eq. (1) and taking the reciprocal derivative $dV/dI_{corr} = (nkT/q)I_{corr}^{-1} + R_S$ , the series resistance $R_s$ can be extracted at the y-axis intercept of the $dV/dI_{corr}$ versus $(I_{corr})^{-1}$ plot, as shown in Fig. 4(c). By extrapolating the semi-logarithmic plot of $I_{corr}$ versus $V$-$R_S I_{corr}$, the reverse saturation current $I_0$ can be evaluated from

#255681 Received 14 Dec 2015; revised 12 Feb 2016; accepted 19 Feb 2016; published 23 Feb 2016
© 2016 OSA

the y-axis intercept (Figures are not shown here). Moreover, the Arrhenius activation energy was estimated from a fit of temperature dependent $I_0 = I_{00}\exp(-E_A/kT)$, where $I_{00}$ is a constant, as shown in Fig. 4(d). The GeSn diode parameters are summarized in Table 2.

**Table 2. Series Resistance, Shunt Resistance, Reverse Saturation Current, and Activation Energy at 77 K and 300 K**

| Device | 77 K | | | 300 K | | | $E_A$ (eV) |
|---|---|---|---|---|---|---|---|
| | $R_S$ (Ω) | $R_{Sh}$ (kΩ) | $I_0$ (A) | $R_S$ (Ω) | $R_{Sh}$ (kΩ) | $I_0$ (A) | |
| 7% Sn, 250 µm | 26.2 | 599 | $6.4 \times 10^{-8}$ | 55.5 | 0.85 | $2.2 \times 10^{-5}$ | 0.14 |
| 7% Sn, 500 µm | 19.6 | 101 | $2.4 \times 10^{-7}$ | 44.7 | 0.22 | $5.9 \times 10^{-5}$ | 0.13 |
| 10% Sn, 250 µm | 35.6 | 23.0 | $3.2 \times 10^{-6}$ | 40.6 | 0.21 | $6.9 \times 10^{-5}$ | 0.13 |
| 10% Sn, 500 µm | 33.2 | 4.70 | $2.6 \times 10^{-5}$ | 41.3 | 0.08 | $8.1 \times 10^{-5}$ | 0.10 |

As the Sn composition increases, the shunt resistance $R_{sh}$ decreases while the reverse saturation current $I_0$ increases. On the other hand, devices with larger mesa size feature lower shunt resistance and higher saturation current compared to those with smaller mesa size. There is no clear trend for the series resistance $Rs$, which ranges from 19.6 Ω (7% Sn, 500 µm) to 35.6 Ω (10% Sn, 250 µm) at 77 K and from 40.6 Ω (10% Sn, 250 µm) to 55.5 Ω (7% Sn, 250 µm) at 300 K. It is desirable to have small series resistance in a photodiode. For our samples, the high series resistance might be attributed to the relatively thin n-type Ge contact layer (50 nm cap layer). In contrast with $R_S$, infinite parallel shunt resistance $R_{sh}$ is desirable in a photodiode since it reduces the thermal noise effect. A parallel shunt resistance from 100 to 600 kΩ and 5 to 23 kΩ at 77 K and from 220 to 850 Ω and 84 to 214 Ω at 300 K was obtained for 7 and 10% Sn devices, respectively. The lower value of shunt resistance with the higher Sn-composition device signals the existence of the leakage current. The device with larger perimeter featuring lower shunt resistance was observed as expected. Similar photodiode behavior has been reported for InGaAs, extended-InGaAs, and short-wave HgCdTe detectors [25]. From the temperature-dependent reverse saturation current, the Arrhenius activation energies $E_A$ for both devices were extracted. According to the theoretical study, the $E_A \sim E_g/2$ indicates that the Shockley-Hall-Read recombination is the main source of dark current [26]. For the $E_A$ obtained in this study, their values ranging from 0.1 to 0.14 eV were much lower than $E_g/2$ (~0.28 and 0.24 eV for 7 and 10% Sn devices, respectively), which seems to suggest a process of defect-assisted tunneling and/or thermionic tunneling [19,27,28].

The reverse dark current density was further investigated to estimate the surface leakage current, which is proportional to the perimeter of the device under test. At −1 V, $J_{surf}$ were extracted to be ~2 mA/cm and 40 mA/cm for 7 and 10% Sn sample at 77 K, respectively. As the temperature increases to 300 K, these values reach 18 mA/cm and 100 mA/cm. The relatively high surface leakage current density is mainly due to two causes: 1) no surface passivation technique was applied on the sidewalls of photodiode device; and 2) the narrowed bandgap of the $Ge_{1-x}Sn_x$ alloy leads to more thermally excited carriers. The dark current can be reduced by a passivation technique either using Si [20] or yttrium-doped $GeO_2$ [29] as the passivation layer.

#255681 Received 14 Dec 2015; revised 12 Feb 2016; accepted 19 Feb 2016; published 23 Feb 2016
© 2016 OSA

## 5. Spectral response

Figures 5(a) and 5(b) show the spectral response of 7 and 10% Sn photodiode detectors in the temperature range from 300 to 77 K. The red shift of absorption edge as the temperature increases was observed for both devices. The 7% Sn device exhibits a cutoff wavelength of 2.0 and 2.2 μm at 77 and 300 K, respectively. Such cutoff wavelengths are way beyond the Ge band-to-band absorption edge (1.55 μm), indicating that the photoresponse beyond 1.55 μm is mainly contributed by the GeSn absorption. For the 10% Sn device, the observed photoresponse extended to 2.3 and 2.6 μm at 77 K and 300 K, respectively. This longer wavelength coverage is due to the reduced bandgap for the increased Sn composition as expected by Vegard's law interpolation of Ge and Sn [30]. The signal distortion at 1.8-1.9 μm is due to the atmospheric absorption that occurred for all of devices regardless of the Sn composition and temperature.

The cutoff wavelength of a detector can be defined by active region's absorption coefficient. This value is normally evaluated from extinction coefficient and refractive index determined from spectroscopic ellipsometry measurement [31]. However, it is possible to determine the absorption coefficient experimentally from the photoresponse measurement as described in [6,32]. The photoresponse intensity is:

$$P_{PR} = P_{INC} \times (1 - e^{-\alpha x}) \tag{2}$$

where $P_{INC}$ is the incident light intensity, $\alpha$ is absorption coefficient, and $x$ is the device thickness. Near the bandgap, the absorption coefficient can be expressed as:

$$\alpha \propto [h\nu - E_g \pm E_p]^m \tag{3}$$

where $h\nu$ is the incident photon energy, $E_g$ is the bandgap of the material, $E_p$ is the energy of the phonon that allows for indirect bandgap transition, and $m$ is a constant. Since the thickness of the GeSn active layer (200 nm) is much smaller than the light penetration depth, i.e., $\alpha x \ll 1$, then Eq. (2) can be reduced to $P_{PR} = C \times \alpha$. A semi-logarithmic plot of spectral response intensity versus the photon energy can be used to extract the $m$ values, as shown in Figs. 5(c) and 5(d) for the 7 and 10% Sn photodiode devices. Based on the study of band-to-band transition, the $m$ is generally equal to 2 and 1/2 for the indirect and direct bandgap transition, respectively. The $m$ values in this study were extracted as 1.11 for the 7% Sn device, and 0.61 for the 10% Sn device at 300 K. This can be explained as following: for the 7% Sn device, the energy separation between indirect and direct bandgap is small (28 meV), therefore the absorption edges of indirect and direct bandgap transition cannot be identified, resulting in the "overall" absorption edge with $m$ value between the 2 and 1/2; while for the 10% Sn device, since the GeSn alloy with 10% Sn has been identified as a direct bandgap material, the Sn composition of 9.24% in this study is very close to the indirect-to-direct transition point. Although the sample is still an indirect bandgap material, the absorption arising from direct bandgap transition dominates the spectral response, leading to the $m$ value of 0.61 which is close to 1/2. Moreover, as temperature decreases, the $m$ values stay almost unaltered for both devices, indicating the identical absorption mechanism at each temperature.

#255681 Received 14 Dec 2015; revised 12 Feb 2016; accepted 19 Feb 2016; published 23 Feb 2016
© 2016 OSA

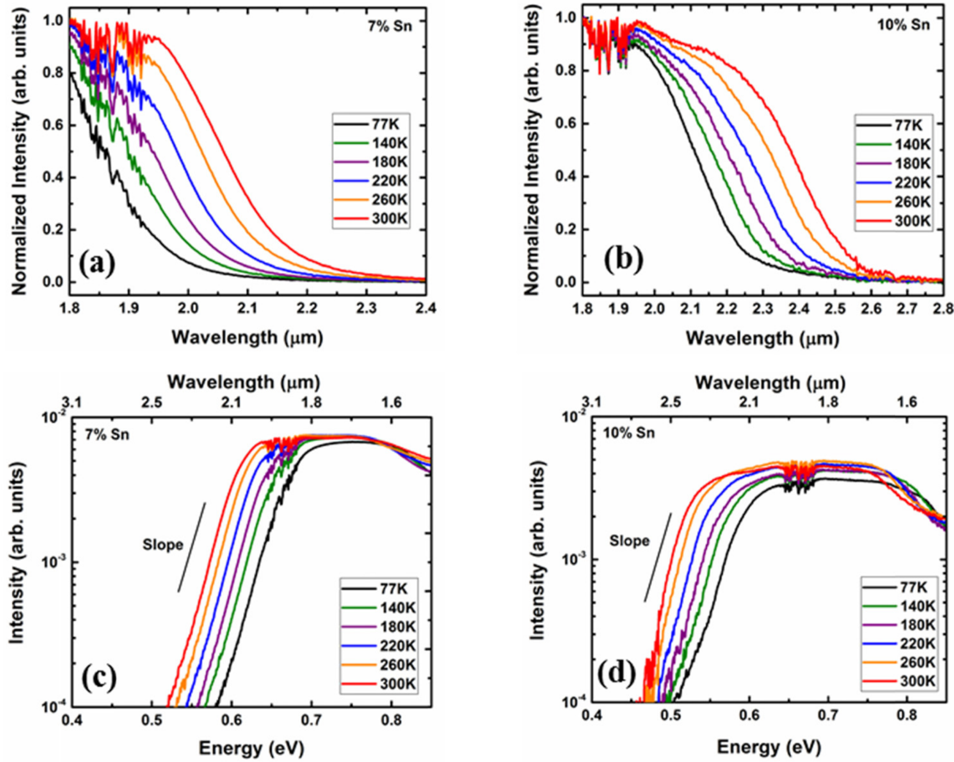


Fig. 5. Temperature dependent spectral response of (a) 7% and (b) 10% Sn photodiode. Temperature dependent absorption edge of (c) 7% and (d) 10% Sn photodiode. The value of slope indicates the absorption mechanism.

## 6. Temperature dependent responsivity

The responsivity was measured at 1.55 μm with a normal incidence laser beam. The I-V curves measured under dark and laser illumination at each temperature were used to calculate the responsivity value verse the bias voltage. Responsivity can be interpreted as [10,32]:

$$R = \frac{\lambda}{1.24}(1-r)\eta_r(1-e^{-\alpha x}) \tag{4}$$

where $\lambda$ is the wavelength, $r$ is the Fresnel loss, $\eta_r$ is the collection efficiency, $\alpha$ is the absorption coefficient, and $x$ is the thickness of absorption layer.

Figures 6(a) and 6(b) show the responsivity at 1.55 μm of 7 and 10% Sn photodiode devices at the temperatures ranging from 77 to 300 K. The peak responsivities of 0.3 and 0.19 A/W were obtained at 300 K with 0.1 V reverse bias voltage for 7 and 10% Sn samples respectively. As the reverse bias voltage increases, the responsivity decreases. This may be due to the higher leakage current under higher reverse bias voltage. In addition, it has been reported that the voltage dependent change of absorption coefficient as a result of the Franz-Keldysh effect could affect the responsivity [33]. At 1 V reverse bias voltage, the responsivities reduce to 0.15 and 0.07 A/W for 7 and 10% Sn devices, respectively. The temperature dependent responsivity shows the monotonically decreased value at lower temperatures for both devices. The increasing bandgap with the decreasing temperature is responsible for this with the absorption coefficient drop. Moreover, in general the responsivity of the 7% Sn sample is higher than that of the 10% Sn sample. This is mainly due to the higher material quality of the 7% Sn sample, which was confirmed by the material

#255681 Received 14 Dec 2015; revised 12 Feb 2016; accepted 19 Feb 2016; published 23 Feb 2016
© 2016 OSA

characterization. The lower material quality of the 10% Sn sample leads to the enhanced non-radiative recombination such as Shockley-Read-Hall recombination (recombination through the defect levels), which reduces the extraction efficiency of photo generated carriers, resulting in lower responsivity.

According to Eq. (4), responsivity could be improved by reducing the Fresnel optical reflection losses with an appropriate antireflection coating and by increasing the GeSn layer thickness. However, the increase in $x$ decreases the response speed of the detector [24,34]. The tradeoff between high responsivity and high-speed response should be taken into account in the design of the photodetector.

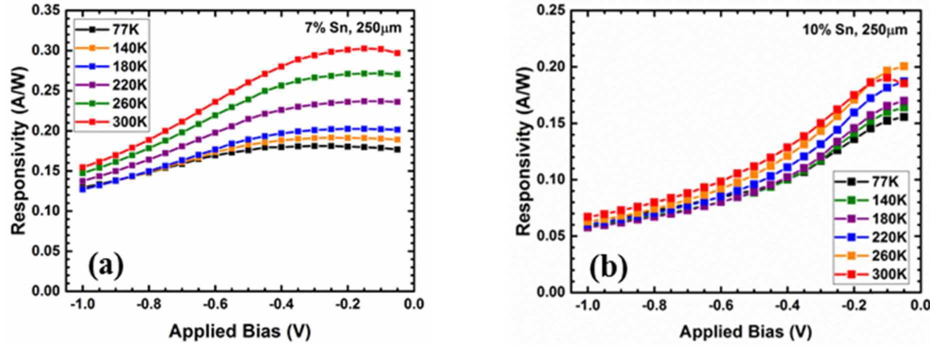


Fig. 6. Temperature dependent responsivity measured at 1.55 μm of (a) 7% Sn and (b) 10% Sn devices with mesa size of 250 μm in diameter.

## 7. Specific detectivity D*

### *7.1 Noise analysis*

The figure-of-merit most commonly used to compare individual detector is specific detectivty D* since it normalizes detector area and uses an equivalent noise bandwidth of 1 Hz. D* can be expressed as:

$$D^* = \frac{\sqrt{A}}{NEP} = \frac{R\sqrt{A\Delta f}}{\sqrt{I_n^2}} \tag{5}$$

where $A$ is the area of the detector, $NEP$ is noise equivalent power, $R$ is responsivity, $\Delta f$ is the bandwidth, and $I_n^2$ is mean squared noise current in the bandwidth. For an ideal photodiode, the noise current is generally composed of thermal fluctuations (Johnson-Nyquist) and shot noise [24]. Flicker or 1/f noise is excluded since its contribution is not significant for measurement conditions above 1 Hz. Therefore, $I_n^2 = I_{thermal}^2 + I_{shot}^2$. The thermal noise follows $I_{thermal} = \sqrt{4kT\Delta f / R_0}$, where $k$ is the Boltzmann constant, $T$ is absolute temperature, $\Delta f$ is the bandwidth, and $R_0$ is the resistance. The shot noise is related to dark current and photocurrent caused by incident light source. It can be described as $I_{shot} = \sqrt{2q(I_{dk} + I_{ph})\Delta f}$, where $q$ is the electron charge, $I_{dk}$ is the dark current, and $I_{ph}$ is the photocurrent. The photocurrent was extracted from the responsivity measurement. In this study, noise bandwidth was set by configuring the time constant and slope/oct of the lock-in amplifier to 100 ms and 18 dB/oct, respectively. The dark current and photocurrent for the devices with 250 μm in diameter are listed in the Table 3.

#255681 Received 14 Dec 2015; revised 12 Feb 2016; accepted 19 Feb 2016; published 23 Feb 2016
© 2016 OSA

**Table 3. Dark current and photocurrent at different reverse bias voltages**

| Temperature (K) | Applied voltage (V) | 7% Sn | | 10% Sn | |
|---|---|---|---|---|---|
| | | Dark current (A) | Photocurrent (A) | Dark current (A) | Photocurrent (A) |
| 300 | −0.2 | $9.55 \times 10^{-5}$ | $4.81 \times 10^{-6}$ | $6.42 \times 10^{-4}$ | $2.79 \times 10^{-6}$ |
| | −1 | $2.82 \times 10^{-3}$ | $2.47 \times 10^{-6}$ | $8.97 \times 10^{-3}$ | $1.07 \times 10^{-6}$ |
| 77 | −0.2 | $3.03 \times 10^{-6}$ | $2.88 \times 10^{-6}$ | $6.55 \times 10^{-5}$ | $2.17 \times 10^{-6}$ |
| | −1 | $1.12 \times 10^{-3}$ | $2.07 \times 10^{-6}$ | $4.6 \times 10^{-3}$ | $1 \times 10^{-6}$ |

Generally speaking, since the ideal photodiode features the suppressed dark current, the thermal noise is the main source of detector noise. However, for the $Ge_{1-x}Sn_x$ detector in this study, the shot noise is the dominant source of noise due to the relatively high dark current. Based on the measured temperature dependent I-V characteristic, each noise component can be determined, as summarized in Table 4.

**Table 4. Thermal Noise and Shot Noise of 7 and 10% Sn DHS Photodiodes with Different Diameter Size, Temperature, and Applied Voltage.**

| Device | Thermal Noise ($A*Hz^{-1/2}$) | | Shot Noise ($A*Hz^{-1/2}$) | | | |
|---|---|---|---|---|---|---|
| | | | −0.2 V | | −1 V | |
| | 77 K | 300 K | 77 K | 300 K | 77 K | 300 K |
| 7% Sn, 250 µm | $8.4 \times 10^{-14}$ | $4.4 \times 10^{-12}$ | $1.4 \times 10^{-12}$ | $5.7 \times 10^{-12}$ | $1.9 \times 10^{-11}$ | $3.0 \times 10^{-11}$ |
| 7% Sn, 500 µm | $2.1 \times 10^{-13}$ | $8.7 \times 10^{-12}$ | $2.8 \times 10^{-12}$ | $1.2 \times 10^{-11}$ | $3.4 \times 10^{-11}$ | $4.5 \times 10^{-11}$ |
| 10% Sn, 250 µm | $4.3 \times 10^{-13}$ | $8.8 \times 10^{-12}$ | $4.7 \times 10^{-12}$ | $8.6 \times 10^{-12}$ | $3.8 \times 10^{-11}$ | $5.4 \times 10^{-11}$ |
| 10% Sn, 500 µm | $9.5 \times 10^{-13}$ | $1.4 \times 10^{-11}$ | $1.4 \times 10^{-11}$ | $2.4 \times 10^{-11}$ | $5.2 \times 10^{-11}$ | $7.0 \times 10^{-11}$ |

At 77 K, the thermal noise is two or three orders of magnitude less than the shot noise at various applied bias voltages. As temperature increases, both thermal and shot noise increase with the thermal noise rising more rapidly than shot noise. The thermal noise increases about two orders of magnitude while the shot noise increases less than one order of magnitude as the temperature increases from 77 to 300 K. At 300 K, the thermal noise is only one order of magnitude smaller than the shot noise at −1 V, and is almost equal to the shot noise at −0.2 V. Therefore for the calculation of D*, both thermal noise and shot noise were considered even at lower temperatures.

### *7.2 Specific detectivity D**

Specific detectivity D* of $Ge_{1-x}Sn_x$ photodiode detectors was determined by using 1 Hz equivalent noise bandwidth, the device area, the calculated noises and the measured responsivity. Figures 7(a) and 7(b) show the D* of 7 and 10% Sn devices with a diameter of 250 µm from 77 K to 300 K. The peak D* of $4 \times 10^9$ and $2.4 \times 10^9$ $cmHz^{1/2}W^{-1}$ for 7 and 10% Sn devices were obtained at 77 K, respectively. Although the responsivity exhibits the smallest value at this temperature, the dark current significantly decreases, resulting in the reduced noise power, and consequently the improved D* value compared to that at 300 K. The lower peak D* of the 10% Sn device compared to that of the 7% Sn device is due to the smaller responsivity and larger noise power. Moreover, the D* of devices with different mesa sizes show the very close values under the same temperature and bias voltage, suggesting the uniform device quality of $Ge_{1-x}Sn_x$ detectors.

#255681 Received 14 Dec 2015; revised 12 Feb 2016; accepted 19 Feb 2016; published 23 Feb 2016
© 2016 OSA

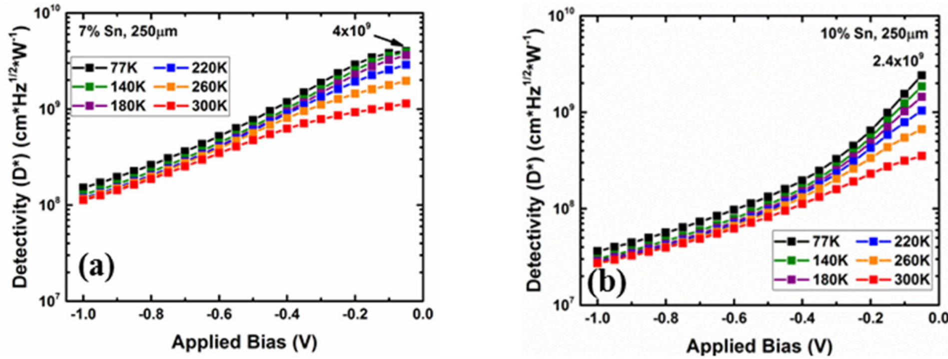


Fig. 7. Temperature dependent specific D* of (a) 7% Sn and (b) 10% Sn device with mesa size of 250 µm in diameter.

Spectral D* of 7 and 10% Sn photodiodes (measured at 0.1 V reverse bias voltage) is shown in Fig. 8 to directly compare with D* of other market-dominating detectors that use Ge, PbS, InAs, and InGaAs technologies. The spectral response absorption edge is extended to 2.6 µm at 300 K for the 10% Sn device, which is comparable to the edge-response of an extended-InGaAs detector at 300 K. Compared to our previous study on GeSn photoconductors [7,9], the spectral D* here has been improved due to the lower dark current of the present GeSn photodiode. The spectral D* of the 7% Sn device at 77 K is only one order of magnitude lower than that of extended-InGaAs detectors. A decrease in the device dark current via a thicker GeSn layer and via application of the passivation technique would dramatically reduce the noise. Moreover, a thicker GeSn layer would enhance the absorption in SWIR. Therefore significantly improved D* of GeSn photodiode detectors can be achieved, making them competitive with commercially available detector technologies in the above-discussed SWIR FPA applications-space.

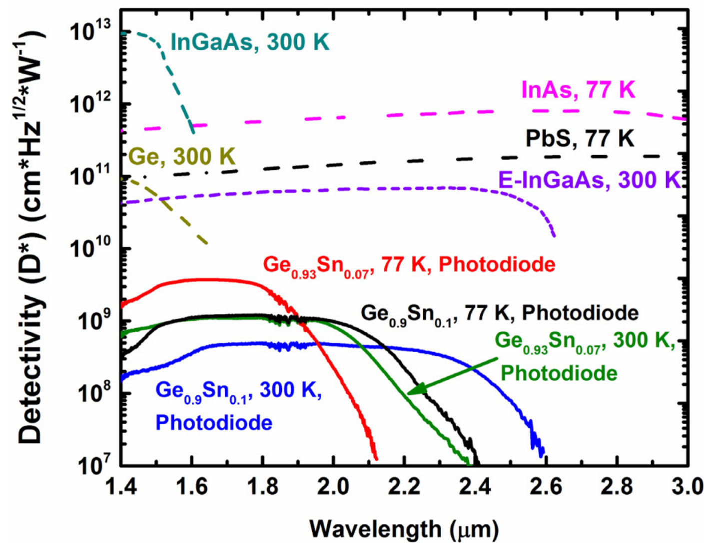


Fig. 8. Spectral D* of 7 and 10% Sn photodiodes measured at 0.1 V reverse bias voltage across a 250 µm-diam device. Other market dominating detectors in same spectral range are plotted for comparison.

#255681 Received 14 Dec 2015; revised 12 Feb 2016; accepted 19 Feb 2016; published 23 Feb 2016
© 2016 OSA

## 8. Conclusion

Systematic studies of 7 and 10% Sn DHS photodiode detectors were conducted at temperatures ranging from 300 to 77 K. The shunt resistance, series resistance, reverse saturation current, and activation energy were extracted from temperature dependent I-V characteristics. A spectral response cutoff wavelength of 2.6 µm was observed for the $Ge_{0.9}Sn_{0.1}$ DHS photodiode at 300 K. Peak responsivities of 0.3 A/W and 0.19 A/W were measured at 300 K for 7 and 10% Sn devices, respectively. With the noise analysis, the peak D* were calculated as $4 \times 10^9$ and $2.4 \times 10^9$ $cmHz^{1/2}W^{-1}$ at 77 K for 7 and 10% Sn devices, respectively. Moreover, spectral D* was plotted along with the market dominating detectors, showing GeSn D* only one order of magnitude lower than those of extended-InGaAs detectors. Considering their CMOS compatibility and capability of monolithic integration on Si, the present GeSn-based detector results project a promising future for GeSn technology towards realization of practical SWIR FPAs.


## Acknowledgments

The work in UA is supported by the National Science Foundation (NSF) (EPS-1003970), the Arktonics, LLC (Air Force SBIR, FA9550-14-C-0044, Dr. Gernot Pomrenke, Program Manager) and DARPA (W911NF-13-1-0196, Dr. Jay Lewis, Program Manager). Drs. R. A. Soref and G. Sun acknowledge support from AFOSR (FA9550-14-1-0196, Dr. Gernot Pomrenke, Program Manager) and from AOARD (FA2386-14-1-4073, Dr. Kenneth Caster, Program Manager).


#255681 Received 14 Dec 2015; revised 12 Feb 2016; accepted 19 Feb 2016; published 23 Feb 2016
© 2016 OSA


131.84.11.215 {ts '2018-05-03 13:25:39'}